Full Control of Polarization in Ferroelectric Thin Films Using Growth Temperature to Modulate Defects

Christian Weymann,* Céline Lichtensteiger, Stéphanie Fernandez-Peña, Aaron B. Naden, Liv R. Dedon, Lane W. Martin, Jean-Marc Triscone, and Patrycja Paruch*

Deterministic control of the intrinsic polarization state of ferroelectric thin films is essential for device applications. Independently of the well-established role of electrostatic boundary conditions and epitaxial strain, the importance of growth temperature as a tool to stabilize a target polarization state during thin film growth is shown here. Full control of the intrinsic polarization orientation of PbTiO₃ thin films is demonstrated—from monodomain up, through polydomain, to monodomain down as imaged by piezoresponse force microscopy—using changes in the film growth temperature. X-ray diffraction and scanning transmission electron microscopy reveal a variation of *c*-axis related to out-of-plane strain gradients. These measurements, supported by Ginzburg–Landau–Devonshire free energy calculations and Rutherford backscattering spectroscopy, point to a defect mediated polarization gradient initiated by a temperature dependent effective built-in field during growth, allowing polarization control not only under specific growth conditions, but ex-situ, for subsequent processing and device applications.

Dr. C. Weymann, Dr. C. Lichtensteiger, Dr. S. Fernandez-Peña,[+]
Prof. J.-M. Triscone, Prof. P. Paruch
Department of Quantum Matter Physics
University of Geneva
24 Quai Ernest-Ansermet, Geneva 4 CH-1211, Switzerland
E-mail: christian.weymann@unige.ch; patrycja.paruch@unige.ch

Dr. A. B. Naden
School of Chemistry
University of St Andrews
Fife, Scotland KY16 9ST, UK

L. R. Dedon,[++] Prof. L. W. Martin
Department of Materials Science and Engineering
University of California at Berkeley
Berkeley, CA 94720, USA

Prof. L. W. Martin
Materials Sciences Division
Lawrence Berkeley National Laboratory
Berkeley, CA 94720, USA

The ORCID identification number(s) for the author(s) of this article can be found under https://doi.org/10.1002/aelm.202000852.

[+]Present address: European Organization for Nuclear Research (CERN), Geneva 23 CH-1211, Switzerland

[++]Present address: Department of Food Science, University of Massachusetts, Amherst, 01003 MA, USA

1. Introduction

In ferroelectric materials, characterized by their remanent electric polarization which can align in one of the available symmetry-equivalent energy-degenerate ground states, control of the intrinsic polarization orientation prior to any application of external electric fields is a longstanding fundamental challenge. For thin films, where the presence of polarization discontinuities and imperfect screening at the surfaces leads to a depolarizing field, tuning of the electrostatic boundary conditions provides a crucial control parameter,[1–3] allowing the intrinsic domain configuration to be modified from monodomain to polydomain through the choice of different electrode materials, the use of dielectric spacers,[4–7] or changes to the chemical environment.[8–10] In addition, asymmetries introduced by epitaxial mismatch strain, substrate morphology or device geometry can also lead to a built-in field in the ferroelectric layer. For example, lattice mismatch relaxation between a relatively thick ferroelectric film and its substrate, inducing strain gradients and a flexoelectric polarization, was shown to produce two different monodomain polarization orientations as a function of growth temperature,[11,12] and in ultrathin films and superlattices an interplay of these different factors can produce complex and fascinating polarization textures including polarization vortices and skyrmion-like bubble domains.[13–15]

Beyond the fundamental interest, this control has important technological implications for ferroelectrics-based applications, such as non-volatile random access memories,[16] devices using ferroelectric tunnel junctions,[17,18] and memristors,[19,20] where an initial defined monodomain state is desirable, and obtaining it intrinsically would eliminate preliminary poling steps, which could be detrimental for certain applications such as surface electrochemistry or catalysis[21,22] by modifying the sample surface.[23,24] In contrast, for applications specifically targeting the added functionalities attendant to domain walls or complex polarization textures, which can strongly modify the dielectric and piezoelectric response[25–27] or present novel properties beyond those of the parent phase,[28] even leading to negative capacitance responses,[29,30] an intrinsic polydomain state may be the goal, and difficult to obtain over large areas, and certainly not without much effort and expense in terms of nanolithography.

**ADVANCED
SCIENCE NEWS**

www.advancedsciencenews.com

**ADVANCED
ELECTRONIC
MATERIALS**

www.advelectronicmat.de

Ideally, what is needed is a mechanism allowing full deterministic control over the intrinsic polarization state, from one monodomain state, through polydomain, to the other monodomain state, reliably, robustly and in general under the different electrostatic and environmental boundary conditions which the sample would encounter during device fabrication and use.

Here, we report such full control over the intrinsic polarization of epitaxial thin films of the canonical ferroelectric PbTiO₃ (PTO), showing that a monodomain "up," polydomain, or monodomain "down" state can be established as a function of increasing growth temperature, under full biaxial strain with no relaxation, independently of the choice of electrostatic boundary conditions, and ex-situ stable for at least two years. We demonstrate this extremely robust control in four series of samples with different back electrodes, grown at a range of temperatures and characterized by piezoresponse force microscopy (PFM), x-ray diffraction (XRD), transmission electron microscopy (TEM) and Rutherford backscattering spectroscopy (RBS). Our results are consistent with a microscopic mechanism of a temperature driven effective internal field during growth, resulting in a varying built-in field across the film, which then stabilizes the target polarization state.

2. Experimental Results

As a model system for this study, we selected the tetragonal ferroelectric PbTiO₃, extensively characterized via ab-initio

and mean-field modeling,[31–33] and a versatile research platform in which the effects of electrostatic boundary conditions were demonstrated[5,7,34,35] and complex polarization textures investigated.[13–15]

Using off-axis radio-frequency magnetron sputtering[36] four series of 50 nm thick PbTiO₃ samples were epitaxially grown on (001)-oriented SrTiO₃ single-crystal substrates, either Nb-doped or undoped and with a bottom electrode of LaNiO₃ or SrRuO₃, the latter in one series capped with an additional thin SrTiO₃ layer to modify the depolarizing field, as schematically illustrated in **Figure 1**. For each series, the deposition conditions were kept the same, except for the growth temperature, which was varied between 530 and 590 °C. Due to their low thickness and the low in-plane lattice mismatch between the SrTiO₃ substrate and the a-axis of tetragonal PbTiO₃, all samples were fully strained, as demonstrated by reciprocal space XRD maps (see, for example, Figure S1, Supporting Information), with no indication of relaxation of the in-plane lattice parameter. The slight bi-axial compressive strain ensured that the tetragonal c-axis, and hence the film polarization, was out-of-plane, with only two orientations possible: up (pointing away from the substrate) or down (pointing toward the substrate). Although there are some variations in sample quality, they cannot trivially explain our observations, see Discussion S1, Supporting Information.

In each sample, the intrinsic polarization state was investigated and compared to a well defined artificial domain structure of alternating down/up/down/up/down stripes written with a biased scanning-probe microscope tip. As can be seen
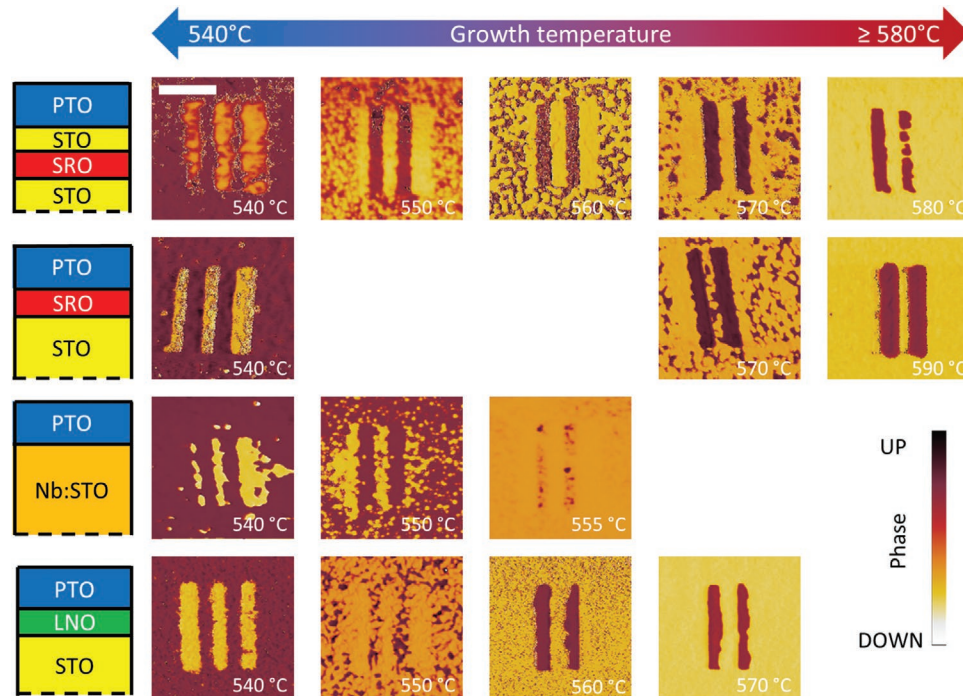

Figure 1. Growth temperature control of polarization. PFM phase for samples grown at different growth temperatures for various back electrodes. The white scale bar in the upper left image is 400 nm and all images are shown at the same scale. The direction of background polarization was determined for each sample by writing striped domains of know orientation. Samples in the same column were deposited at temperatures within 5 °C from each other. The back electrodes used were, from top to bottom : 22 nm of SrRuO₃ (SRO) capped by 2 nm of SrTiO₃ (STO), SrRuO₃ without the capping layer, the conductive Nb:SrTiO₃ substrate, and 8 nm of LaNiO₃ (LNO). All electrodes and capping layers were deposited in-situ. In each series, the as-grown polarization state follows the same trend: monodomain up for low growth temperatures, polydomain for intermediate growth temperatures and monodomain down for high growth temperatures.
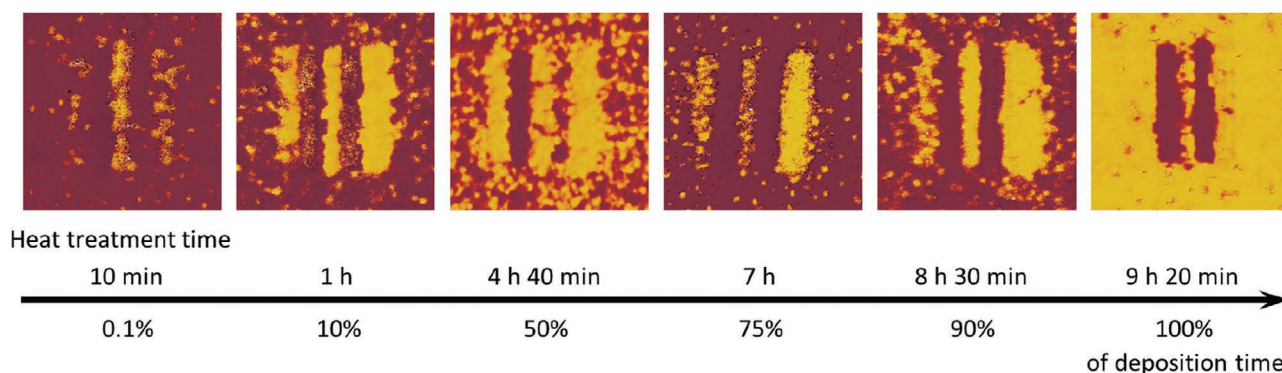
**ADVANCED
SCIENCE NEWS**
www.advancedsciencenews.com

**ADVANCED
ELECTRONIC
MATERIALS**
www.advelectronicmat.de

Figure 2. Effect of in-situ heat treatment on polarization. PFM images of samples grown at a low growth temperature (corresponding to a monodomain up polarized state) and subsequently heated to a higher temperature (corresponding to a monodomain down polarized state) in-situ for various durations. The usual control pattern was written in the center of the images. Even for very short heating times (with respect to the total deposition time of 9 h and 20 min), the samples exhibit some down domains. After a sufficiently long heating time, a down polarized state is achieved. This suggests that we can control the intrinsic polarization state by heating the samples at low pressure.

in Figure 1 the four series all present the same trend, independently of the choice of bottom electrode: samples grown at lower temperatures are fully up-polarized, and samples grown at higher temperatures are fully down-polarized, with a polydomain state for intermediate growth temperatures.

To better understand the origin of this phenomenon, we then tested if the high-temperature vs. low-temperature polarization state was only established during growth, or if it could be modified subsequently using temperature alone. We grew a series of samples with $LaNiO_3$ back electrodes at low growth temperature (corresponding to a monodomain up configuration) which were then heated in-situ, after completion of the growth process, and for varying times to the (higher) temperature corresponding to a monodomain down configuration. As **Figure 2** shows, even after a very short heating time, down polarized domains appeared in the up polarized matrix. For a sufficiently long heating time, a down polarized state was achieved. This suggests that the duration of the sample exposure to high temperatures is more critical to the intrinsic polarization state than the fact that this exposure happens specifically during growth.

While previous studies have demonstrated that an intrinsically monodomain polarization state is direct evidence of an internal bias in the sample,[7] favoring one polarization over the other, only one of the two possible monodomain states was ever stabilized for a given choice of electrode and film thickness. In contrast, the robustness of the phenomenon observed here indicates that independently of interface effects, the internal bias changes sign solely due to growth temperature.

To further investigate this change in the internal bias, we performed switching spectroscopy PFM (SSPFM)[37] measurements of the local polarization-voltage hysteresis at multiple points in each sample. The built-in voltage, defined as the shift of the hysteresis loop with respect to zero bias, was extracted for each of these points and used as statistical estimate of the internal bias. The variation of the built-in voltage, presented in **Figure 3** as a function of growth temperature for the representative series of samples on $LaNiO_3$ back electrodes, indeed shows a significant decrease, changing sign from positive at lower growth temperatures to negative for higher growth temperatures, in agreement with the PFM phase imaging results.

In order to study the crystallographic variations related to the varying polarization states, we employed thin film XRD. XRD diffractograms were taken for all our samples as part of our standard initial characterization. The reciprocal space maps (RSM) around (–103) (see, as an example, Figure S1, Supporting Information) show no relaxation, implying that all our samples are epitaxially strained to the substrates. θ-2θ diffractograms along (001) and (002) (see, **Figure 4**a; Figures S2 and S3, Supporting Information), display Laue oscillations attesting again the high crystalline quality of the films. Interestingly, on many of our diffractograms along (002), we observe an additional peak close to $2\theta = 45.3°$ (see, for example, the blue diffractograms in Figure 4a): this peak is due to double diffraction[38,39] and is a consequence of our atomically smooth interfaces. From the 2θ position of the film peak and from the Laue oscillations, one can determine the c-axis lattice parameter and thickness of the films. We used the MATLAB program InteractiveXRDFit developed in-house to fit all our θ-2θ diffractograms, and rapidly noticed that although our samples are of high crystalline quality, the fits performed using a constant c-axis lattice parameter were not satisfactory.[40]

In all cases, the down polarized samples presented a shoulder on the right side of the main film diffraction peak which we did not observe in the up polarized samples (Figure 4a, and Figure S3, Supporting Information). In fact, in many cases, the up polarized samples present a spectral weight to the left of the main film diffraction peak.

Following the argument in ref. [41] that any mechanism to relax strain would depend on strain, to a first approximation, the out-of-plane lattice parameter in a strained film can be anticipated to follow an exponential relationship $c(n) = c_0 + a\exp(n/b)$, where $c(n)$ is the c-axis lattice parameter of the nth unit cell above the interface with the electrode. The results are shown in Figure 4.

This very simple model produces simulations that closely match the main features of the experimental diffractograms (see Figure S5, Supporting Information, for details),
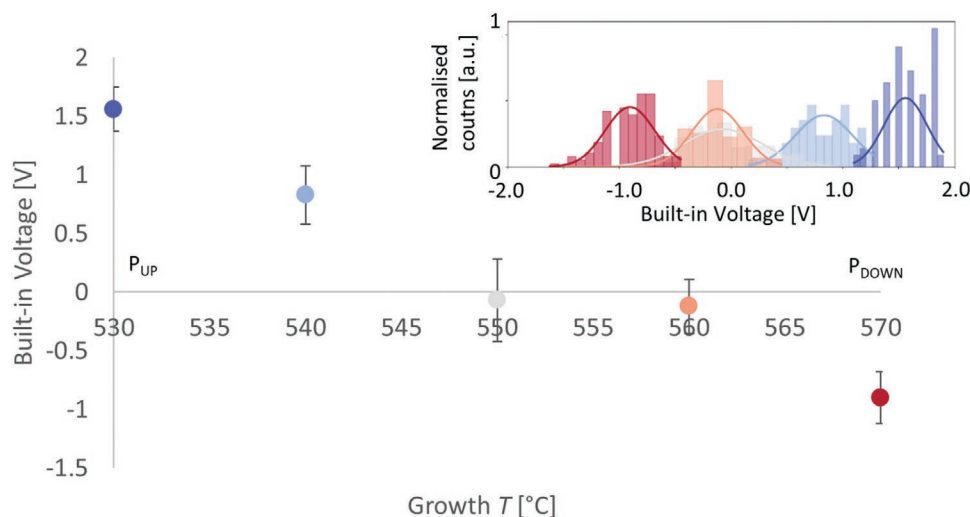
Figure 3. Effect of growth temperature on built-in voltage. SSPFM measurements of built-in voltage in each sample of the series grown on $LaNiO_3$. The inset shows the distribution of shifts of local hysteresis loops (see Figure S4, Supporting Information) with respect to the origin for each sample, and Gaussian fits to that data. The main graph shows the fitted averages and standard deviations. The built-in voltage goes from positive at low growth temperature, which favors the up polarized state, to negative at high growth temperature, which favors the down polarized state, in line with our PFM imaging results.

demonstrating a gradient in the c-axis parameter throughout the film thickness, with very different c-axis distributions in the up versus down polarized films. From the XRD simulations only, it is however not possible to discriminate between the diffractograms obtained with $c(n) = c_0 + a \exp\left(\frac{n}{b}\right)$ and

$c(n) = c_0 + a \exp\left(\frac{\text{top layer number} - n}{b}\right)$, that is, the simulations for two films where one is the mirror image of the other with the top layer becoming the bottom layer and vice-versa, are equivalent.

To resolve this issue, we performed scanning transmission electron microscopy (STEM) measurements on the two samples
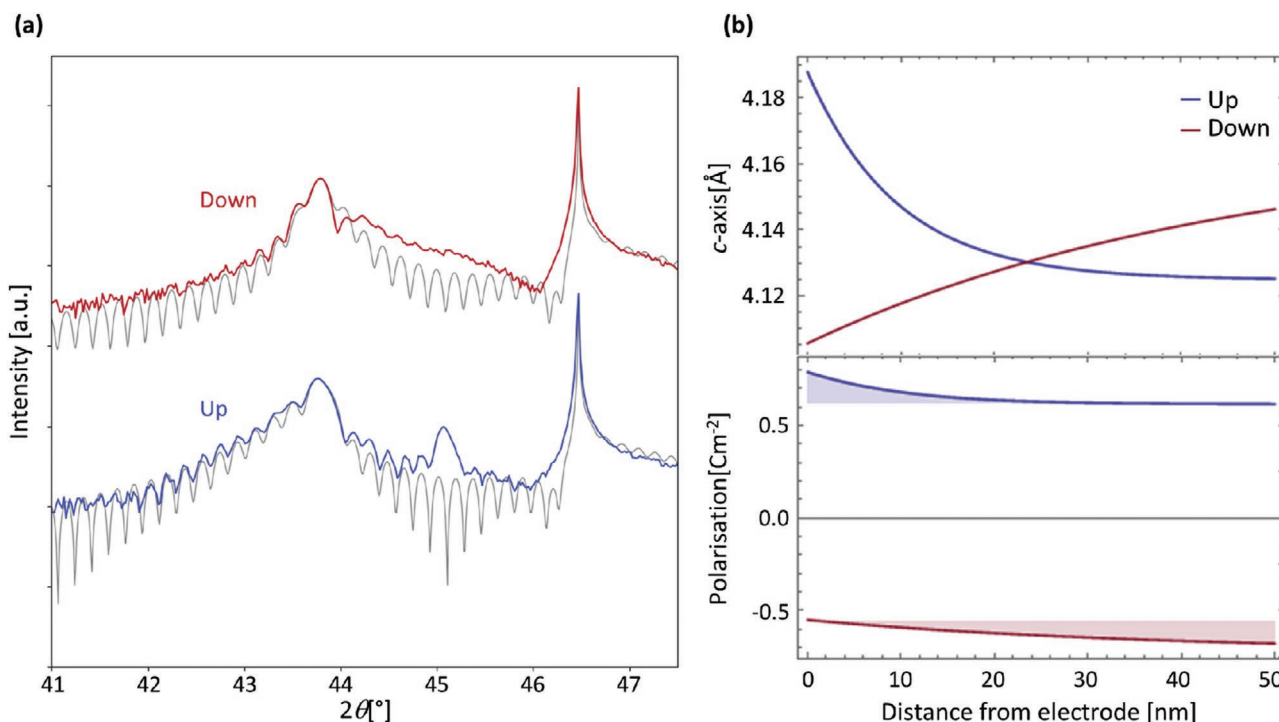

Figure 4. Strain and polarization from XRD. a) Example of $\theta - 2\theta$ XRD spectra around the (002) peak of both the film and the substrate, for one up polarized and one down polarized film on $LaNiO_3$. As in all our series, the high temperature grown, down polarized film shows a distinctive shoulder to the right of the sample peak. Spectra fitted to the data are shown in gray. b) c-axis distribution obtained from the fit to the XRD spectra in (a) and corresponding polarization profiles obtained from the GDL calculation.

**ADVANCED
SCIENCE NEWS**

www.advancedsciencenews.com

**ADVANCED
ELECTRONIC
MATERIALS**

www.advelectronicmat.de

shown in Figure 4, which were grown on LaNiO$_3$, one at the low end of the growth temperature window, and therefore polarized up, and one at the high end of the growth temperature window, and therefore polarized down. Representative atomic resolution high angle annular dark field (HAADF) images are shown in Figure S6, Supporting Information, and the in- and out-of-plane lattice constants were extracted via Gaussian fitting to the atomic columns (see experimental section). To minimize errors, we averaged the measurements over several images collected from different regions. Due to the large field of view, the uncertainty in these measurements is relatively large at ±3 pm based on the 1σ standard deviation. While evidently not as precise as XRD, these measurements nevertheless confirm the presence of gradients in the c-axis lattice parameter throughout the film thicknesses and their direction, in addition to confirming constant a-axis lattice parameters. In the down polarized sample, c increases from bottom to top whereas in the up polarized film c rapidly decreases from a maximum of c within the first few nm of PTO film before remaining largely constant for the rest of the film thickness. Applying these observations of the overall trends to the XRD data, a close fit to the experimental data can be observed in Figure 4a. The fitted c-axis profiles are shown in Figure 4b and show strong agreement (within the measurement error) with the STEM measurements shown in Figure S6, Supporting Information.

These structural measurements are interesting since there is a strong strain-to-polarization coupling in oxide ferroelectrics. We can therefore estimate the polarization inside our films from the strain profiles obtained above, using a Gibbs free energy expansion. We will focus on the monodomain end members of our study, and therefore neglect the effects of in-plane inhomogeneities of the polarization present in polydomain samples. Following ref. [42], the Gibbs free energy in our films is given by

$$G = \int_0^t [a_3 P^2 + a_{33} P^4 + a_{333} P^6$$
$$+ \frac{1}{2} c_{11}(2u_m^2 + e_3^2) + c_{12}(u_m^2 + 2u_m e_3) - q_{11} e_3 P^2 - 2q_{12} u_m P^2$$
$$+ \frac{g_{1111}}{2}\left(\frac{\partial P}{\partial z}\right)^2 - \frac{f_{11}}{2}\left(P\frac{\partial e_3}{\partial z} - e_3\frac{\partial P}{\partial z}\right)$$
$$- PE - 2\sigma u_m] dz \tag{1}$$

where P is the out-of-plane polarization, e_3 is the out-of-plane strain, c_{ij} is the stiffness tensor, q_{ij} is the electrostriction tensor, g_{ijkl} is the correlation energy tensor, f_{ij} is the flexocoupling tensor, E is the electrical field, σ is the in-plane stress and u_m is the mismatch strain with the substrate (**Table 1**). Euler-Lagrange variational minimization of this expression yields

$$c_{11} e_3(z) + 2c_{12} u_m - q_{11} P^2 + f_{11}\frac{\partial P}{\partial z} = 0 \tag{2}$$

which can be solved for $P(z)$, since we know $e_3(z) = \frac{c(z) - c_{ref}}{c_{ref}}$, with c_{ref} the c-axis of the non-ferroelectric reference phase. Upon closer inspection (see Discussion S6, Supporting Information, for further details), we see that we can safely neglect the last term of equation 2 in our case, leading to the closed form

Table 1. Numerical values of the coefficents used in the Gibbs free energy expansion.

Symbol	Value	Units	Reference
a_3	$3.8 \times 10^5 (T - 752)$	JmC^{-2}	[56]
a_{33}	4.229×10^8	Jm^5C^{-4}	
a_{333}	2.6×10^8	Jm^9C^{-6}	
c_{11}	1.746×10^{11}	Jm^{-3}	
c_{12}	0.794×10^{11}		
q_{11}	1.14×10^{10}	JmC^{-2}	
q_{12}	4.63×10^8		
f_{11}	-17	JC^{-1}	[57]

$$P(z) = \pm\sqrt{\frac{1}{q_{11}}(c_{11}e_3(z) + 2c_{12}u_m)} \tag{3}$$

which is plotted in Figure 4b.

Note that this result is agnostic of any electrical fields the sample might be subject to, and returns the total polarization, irrespective of what caused it. A built-in field coming from the interface is constant throughout the thickness of the film and results in a constant polarization (and thus a constant c-axis). In our model, the variations in polarization implied by the varying c-axis we measure must therefore come from something else that varies through the film thickness and as a function of growth temperature.

3. Discussion

In their papers, Highland et al.[10,35] have shown that the in-situ equilibrium polarization of a 10 nm PbTiO$_3$ thin film with SrRuO$_3$ bottom electrode depends on temperature and oxygen partial pressure. For high partial pressures, the film is up polarized, whereas it is down polarized for low partial pressures. Their observations are explained by the preferential screening of the up polarization by oxygen ions, whereas the down polarization is preferentially screened by oxygen vacancies at the surface of the film. In this way, high oxygen partial pressures stabilize an up polarized state, and low oxygen partial pressures stabilize a down polarized state. Interestingly, in the intermediate partial pressure regime, the polarization orientation depends on the temperature. Our growth conditions fall exactly in this intermediate regime, where both polarization orientations can be stable depending on temperature. Our observations are thus compatible with the work of Highland et al. for the establishment of the polarization configuration in-situ, but in our case there must be an additional mechanism to then stabilize this configuration ex-situ.

One possible explanation would be the presence of a gradient of composition that develops during growth or during the post-growth in-situ heat-treatment, which then freezes in and hence stabilizes the polarization configuration. It is well known that chemical species mobility depends exponentially on temperature.[43] Compositional changes and gradients have also previously been shown to produce large built-in fields.[44]
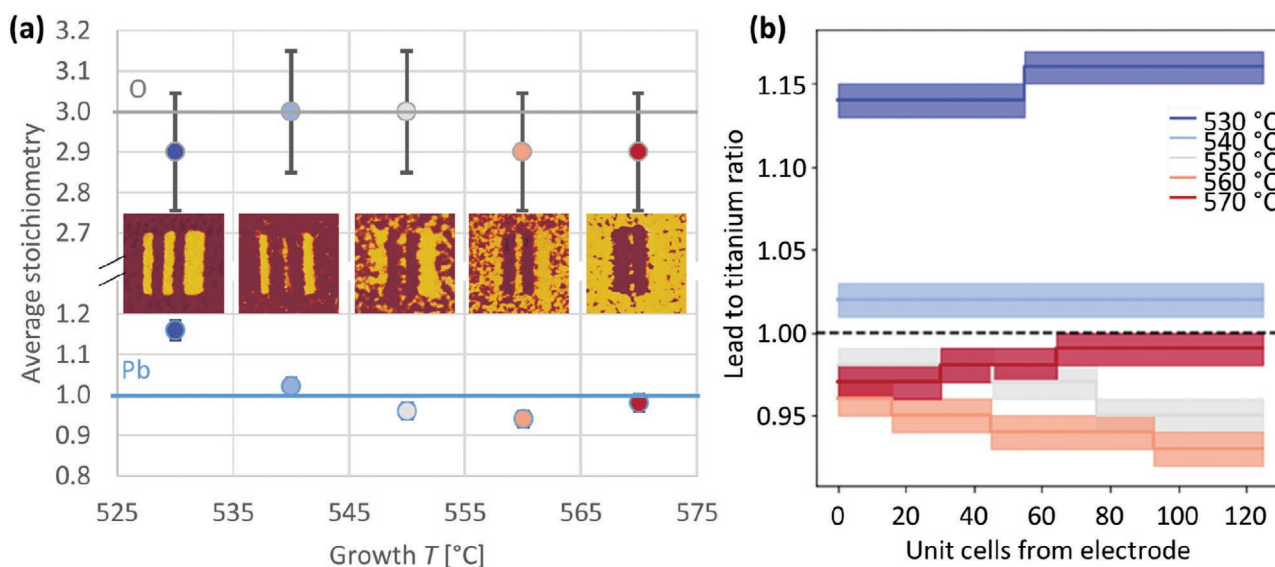
Figure 5. RBS measurements of stoichiometry in five samples grown on LaNiO$_3$ at growth temperatures in the range from 530 to 570 °C. a) Average lead and oxygen content. Titanium was assumed to always be stoichiometric and used as a reference. Error bars represent the uncertainty of the fit. The insets show the PFM phase image for each sample, with the control down/up/down/up/down structure written in the middle of the imaged area. Low temperature grown samples are monodomain up, and up to 16% over-stoichiometric in lead, whereas high temperature grown samples are mostly down polarized, and up to 2% lead deficient. Note that the target used was 10% lead rich. RBS is less sensitive to lighter elements, explaining the much larger error bars on the oxygen stoichiometry—these measurements cannot exclude oxygen vacancy densities of the same order as the lead vacancy densities. b) Lead stoichiometry profiles of the PbTiO$_3$ thin films, as a function of growth temperature. Bands represent the uncertainty of the fit. Low and high growth temperature samples are homogeneous within the experimental error, whereas intermediate growth temperature, polydomain samples have significantly less lead at the surface.

Such gradient would be compatible with the observed gradient in *c*-axis. To explore the potential presence of compositional gradients, we measured the stoichiometry of our films through their thickness using RBS (see Figure S8, Supporting Information), with spectra taken on a series of 5 samples grown on LaNiO$_3$ at temperatures ranging from 530 to 570 °C in 10 °C steps, and fitted using the SIMNRA software.[45] As can be seen in **Figure 5**a, these fits confirm that all our samples are close to stoichiometric, except for the sample grown at the lowest temperature which is lead-rich. This is explained by the fact that we use a 10% Pb-rich target to compensate for the well-known lead volatility. This volatility is lower at lower temperature, resulting in a lead-rich film. The observed Pb distribution moreover appears to be slightly inhomogeneous through the film thickness, as can be seen in Figure 5b, with the top surface showing higher levels of Pb deficiency for intermediate growth temperatures, suggesting a small gradient in Pb vacancy concentration in the polydomain samples. These results are in qualitative agreement with element analysis profiles extracted from the TEM (see Figure S9, Supporting Information).

Another possible explanation as to how the polarization direction present in-situ during growth is stabilized ex-situ is the presence of defect dipoles. Indeed, it is reported[46,47] that Pb vacancies are able to form a dipolar divacancy complex with O vacancies, the presence of which is not excluded by the RBS data, and indeed highly probable in perovskite oxide thin films.[48] We could therefore infer that the divacancy complexes stabilize the in-situ polarization configuration by aligning with the direction of polarization present in the film at the time they are formed, and freezing in upon cooling.

To estimate the concentration of defect dipoles that would be required to achieve the variations in polarization deducted from the GLD calculations, we return to the definition of polarization: the spatial density of (defect)-dipole moments. The moment of one dipole is given by the effective charge of the vacancies, calculated in ref. [49] to be 2.28*e*, multiplied by their separation. Chandrasekaran[47] calculated that the energetically favourable position for the vacancies in the dipole are on next nearest neighbour sites, so that their out-of-plane separation is given by the *c*-axis (up to a refining factor of 0.88 measured in ref. [50]). The variation in polarization that cannot be attributed to interface effects is at most 0.2 C m^{-2}. The necessary density of dipoles can now be estimated by dividing this number by the dipole moment of one vacancy dipole, which gives 0.1 dipole per unit cell. Although the assumptions made in these different sources do not necessarily correspond exactly to our experimental set-up, we believe this number to be a valuable order-of-magnitude check of this hypothesis. Indeed, RBS shows lead concentration as low as 0.93 per unit cell, which makes it plausible that the required concentration of defect dipoles could be achieved at least locally.

One key consequence of this hypothesis is that, since the divacancy dipoles are not present everywhere in the same concentration, the internal field the sample is subject to also varies locally. Since this internal field is coupled to the out-of-plane *c*-axis of the unit cell through the polarization, this results in the observed gradient in the *c*-axis.
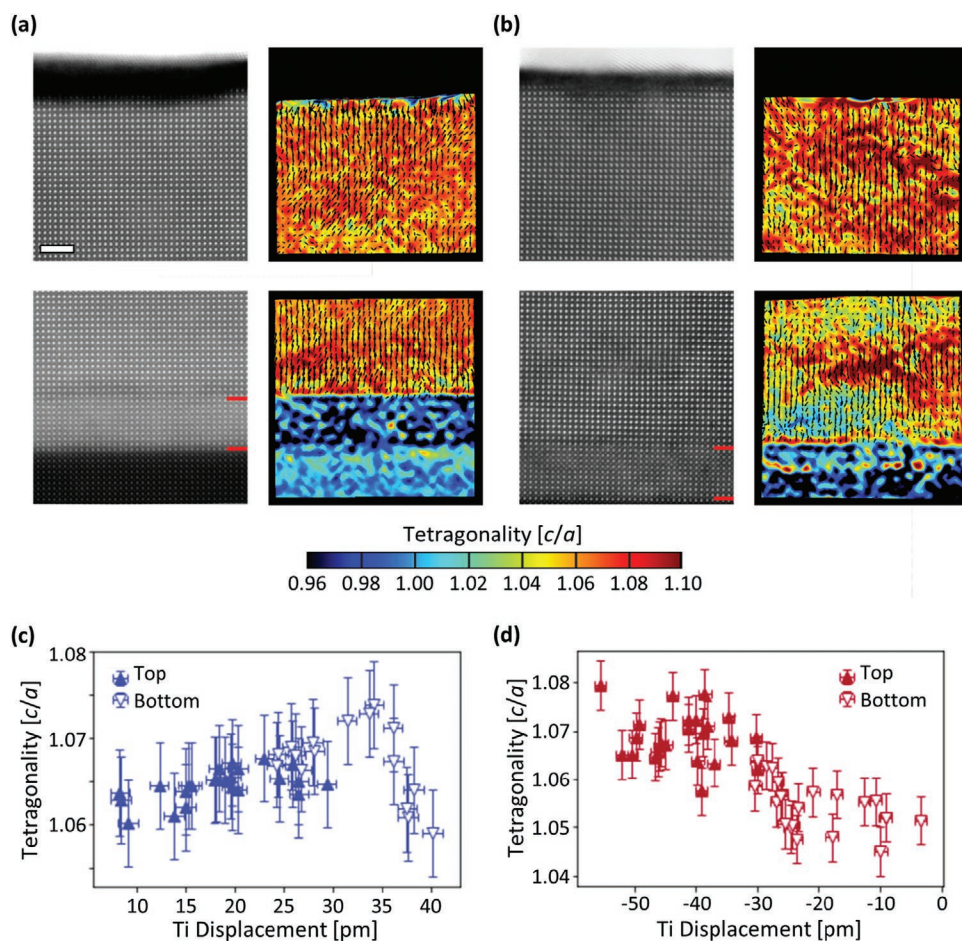
Figure 6. Local strain and polarization mapping. Representative atomic resolution HAADF images (left column) and tetragonality maps (right) from the a) up and b) downward polarized samples presented in Figure 4, Figures S6 and S9, Supporting Information. The top row corresponds to the top of the film and the bottom row to the lower interface with the substrate; the red lines indicate the bottom electrode interfaces. The black arrows overlaid on the tetragonality maps depict the local polarization in the PTO film. c,d) Scatter plots of tetragonality as a function of Ti displacement for the up and downwards polarized samples, respectively. Measurements were taken from several images and averaged to minimize measurement errors; error bars represent the 1σ standard deviation. A general trend of greater Ti displacement (polarization) is observed with increased tetragonality which is lower at the top of the up polarized film in (c) and vice versa in the downward polarized film in (d). The scale bar shown in (a) is the same for all images and corresponds to 2.5 nm.

To assess local variations in polarization, we employed atomic resolution HAADF at the top and bottom interfaces of the two monodomain films. After drift correction and Gaussian fitting to the atom columns (see experimental details), we extracted the local tetragonality—defined by the positions of Pb atom columns—and the displacement of the Ti columns with respect to the central position of the unit cell. The latter is related to the polarization via $P_\alpha = \frac{e}{\Omega} \sum_{j\beta} Z^*_{j\alpha\beta} \Delta u_{j\beta}$ where $\Delta u_{j\beta}$ is the displacement of ion j in the direction β, $Z^*_{j\alpha\beta}$ is the Born effective charge tensor and Ω is the unit cell volume.[51,52] However, without knowing the precise Born effective charges (i.e., valences of the ions), calculating polarization values is likely to be misleading in the present case due to the expected presence of Pb and O vacancies discussed above.

Representative examples for the up and down polarized films are shown in **Figures 6**a and 6b, respectively. The left columns show HAADF images taken from the top and bottom interfaces and the right column shows tetragonality maps with overlaid arrows (black) depicting the local polarization direction, i.e. opposite to the direction of Ti displacement. Both the tetragonality and the displacement show strong local variations, supporting the model of localized defects affecting both. Furthermore, plotting the average tetragonality of one unit cell monolayer against the average out-of-plane displacement of the same monolayer reveals a significant correlation, as shown in Figure 6c,d. This supports the model that changes in polarization cause the gradient in c-axis observed by XRD. Additionally, the top and bottom of both films are clearly clustered, with larger Ti displacement (polarization) and tetragonality at the bottom of the up polarized film and at the top of the down polarized film. These measurements essentially provide 'snapshots' of small regions at the extremities of the film, providing further validation of the c-axis gradients in Figure 4. The only significant exception to this overall behaviour are the first five unit cells above the bottom electrode in the up polarized film (the rightmost points in Figure 6c). These form a layer where

**ADVANCED
SCIENCE NEWS**
www.advancedsciencenews.com

**ADVANCED
ELECTRONIC
MATERIALS**
www.advelectronicmat.de

the tetragonality is low compared to the rest of the film, but the displacement is high. This observation points to a competing effect keeping the tetragonality low in this area which could be related to an interfacial effect. Further investigation is required to fully understand this phenomenon, which could be similar to the interface effects recently reported by other groups.[53,54] However, for the rest of the sample volume, these results are in line with a gradient of lead oxide dipolar vacancies inducing a gradient in polarization, which leads to a gradient in strain.

In summary, we have achieved full deterministic control of the intrinsic polarization state of ferroelectric thin films, independently of the electrostatic boundary conditions. We were able to target the polarization state to be monodomain up, monodomain down, or polydomain, stable ex-situ for at least two years, simply through the use of temperature during film deposition, while maintaining full in-plane epitaxial strain and high surface and crystalline quality. We have shown moreover that this control can be extended beyond the growth stage of the film, and also achieved with a subsequent in-situ annealing. Growth temperature is a particularly easy parameter to access, thus allowing modulation in most of the available growth and deposition systems. Beyond the purely monodomain films, our work offers an additional tuning parameter to create and stabilise extremely small domains with the potential for unusual polarization textures, including nanoscopic bubble domains, vortex and skyrmion-like topologies, opening new perspectives in the fast developing field of domain engineering.

4. Experimental Section

Thin Film Growth: The samples in this study were grown epitaxially using off-axis radio frequency magnetron sputtering. One series was grown directly on unterminated (001)-oriented niobium-doped $SrTiO_3$ substrates, the others were grown on TiO_2 terminated, (001)-oriented, undoped $SrTiO_3$ with various back electrodes. $SrRuO_3$ was deposited at 645 °C in 100 mTorr of O_2/Ar mixture of ratio 3:60 using a power of 80 W. $LaNiO_3$ was deposited at the same temperature as the $PbTiO_3$ in 180 mTorr of a 10:35 O_2/Ar mixture using a power of 50 W. The $SrTiO_3$ spacer layers (when present) and $PbTiO_3$ thin films were deposited at the same temperature varying between 525 and 590 °C in 180 mTorr of a 20:29 O_2/Ar mixture using a power of 60 W. A $Pb_{1.1}TiO_3$ target with a 10% excess of Pb was used to compensate for Pb volatility, while stoichiometric targets were used for all other materials.

XRD Characterization: The X-ray diffraction measurements were performed using a Panalytical X'Pert diffractometer equipped with a monochromator and a triple axis detector.

SPM Characterization: All SPM characterization was performed using an Asylum Research Cypher atomic force microscope. Surface topographies were obtained in tapping mode using Bruker TESPA tips. Piezoresponse force microscopy phase and amplitude were recorded in dual resonance tracking (DART) mode,[55] using conductive Mikromasch HQ:NSC18/Cr-Au coated tips. Excitation amplitudes were typically less than 500 mV per frequency. Alternating stripe domains were written by applying −/+/−/+/− 5 volts to the back electrode while scanning with a grounded metallic tip over an area of 0.5 × 0.5 μm². A larger area of 1 × 1 μm² was then scanned to image both the as grown polarization state and the written stripe domains and compare them. This way the three stripes written in the down state (with −5 V) could be differentiated from the two stripes written in the up state (with +5 V).

SSPFM: SSPFM was performed using the same setup as PFM. Local polarization-voltage hysteresis loops were acquired on each point of a 16 × 16 grid over 2 × 2 μm² using the SPM tip as a top electrode. The saw-tooth potential (as described in ref. [37]) was applied to the tip, with the bottom electrode being grounded. Amplitude signals from the off loops were used for data analysis: the points of lowest amplitude were used as values for the coercive voltages, which were then averaged to give the built-in voltage. Points where the tip-sample contact was obviously bad were filtered out and not considered for further analysis. For more details see ref. [7]. The statistical data were fitted using a Gaussian distribution.

TEM: Cross-sections for STEM were prepared by focused ion beam (FIB) in an FEI Scios dual beam FIB-SEM system at acceleration voltages of 30 kV (coarse milling), 16, 8 (thinning), 5 and 2 kV (final polishing). STEM measurements were performed on an FEI Titan Themis operated at 200 kV. High angle annular dark field (HAADF) images were obtained with inner/outer collection angles of 56.3 and 200 mrad, respectively. Data were corrected for specimen drift and scanning distortion using pairs of images collected at orthogonal scan orientations using the MATLAB procedure reported elsewhere.[58] Atomap[59] was used to extract the tetragonality and Ti displacements by Gaussian fitting to atom columns in the drift-corrected data.

Supporting Information

Supporting Information is available from the Wiley Online Library or from the author.

Data Availability

The data that support the findings of this study are available from the corresponding author upon reasonable request and openly in Yareta at https://doi.org/10.26037/yareta:pzjvvqnsazarvhuk4yr52j6hqy

Conflict of Interest

The authors declare no conflict of interest.

Author Contributions

P.P. and J.-M.T. designed the experiment. C.W., C.L., and S.F.-P. grew the samples and conducted the X-ray diffraction and piezoresponse force microscopy measurements. A.B.N. performed the transmission electron microscopy and the atomic position fitting. L.R.D. carried out the Rutherford back-scattering spectroscopy under the supervision of L.W.M. C.W. carried out the Gibbs free energy expansion calculations. C.W., C.L., and P.P. wrote the manuscript with contributions from all authors. All authors discussed the experimental results and models, commented on the manuscript and agreed on its final version.

Keywords

[1] R. R. Mehta, B. D. Silverman, J. T Jacobs, *J. Appl. Phys.* **1973**, *44*, 3379.

[2] J. Junquera, P. Ghosez, *Nature* **2003**, *422*, 506.

[3] C. Lichtensteiger, P. Zubko, M. Stengel, P. Aguado-Puente, J.-M. Triscone, P. Ghosez, J. Junquera, in *Oxide Ultrathin Films: Science and Technology*, Wiley, New York **2012**, pp. 265–308.

[4] H. Lu, X. Liu, J. D. Burton, C.-W. Bark, Y. Wang, Y. Zhang, D. J. Kim, A. Stamm, P. Lukashev, D. A. Felker, C. M. Folkman, P. Gao, M. S. Rzchowski, X. Q. Pan, C.-B. Eom, E. Y. Tsymbal, A. Gruverman, *Adv. Mater.* **2012**, *24*, 1209.

[5] C. Lichtensteiger, S. Fernandez-Pena, C. Weymann, P. Zubko, J.-M. Triscone, *Nano Lett.* **2014**, *14*, 4205.

[6] G. Liu, J. Chen, C. Lichtensteiger, J.-M. Triscone, P. Aguado-Puente, J. Junquera, N. Valanoor, *Adv. Electron. Mater.* **2016**, *2*, 1500288.

[7] C. Lichtensteiger, C. Weymann, S. Fernandez-Pena, P. Paruch, J.-M. Triscone, *New J. Phys.* **2016**, *18*, 043030.

[8] R. V. Wang, D. D. Fong, F. Jiang, M. J. Highland, P. H. Fuoss, Carol Thompson, A. M. Kolpak, J. A. Eastman, S. K. Streiffer, A. M. Rappe, G. B. Stephenson, *Phys. Rev. Lett.* **2009**, *102*, 047601.

[9] M. J. Highland, T. T. Fister, M.-I. Richard, D. D. Fong, P. H. Fuoss, C. Thompson, J. A. Eastman, S. K. Streiffer, G. B. Stephenson, *Phys. Rev. Lett.* **2010**, *105*, 167601.

[10] M. J. Highland, T. T. Fister, D. D. Fong, P. H. Fuoss, C. Thompson, J. A. Eastman, S. K. Streiffer, G. B. Stephenson, *Phys. Rev. Lett.* **2011**, *107*, 187602.

[11] B. C. Jeon, D. Lee, M. H. Lee, S. M. Yang, S. C. Chae, T. K. Song, S. D. Bu, J.-S. Chung, J.-G. Yoon, T. W. Noh, *Adv. Mater.* **2013**, *25*, 5643.

[12] D. Lee, B. C. Jeon, A. Yoon, Y. J. Shin, M. H. Lee, T. K. Song, S. D. Bu, M. Kim, J.-S. Chung, J.-G. Yoon, T. W. Noh, *Adv. Mater.* **2014**, *26*, 5005.

[13] A. K. Yadav, C. T. Nelson, S. L. Hsu, Z. Hong, J. D. Clarkson, C. M. Schlepütz, A. R. Damodaran, P. Shafer, E. Arenholz, L. R. Dedon, D. Chen, A. Vishwanath, A. M. Minor, L. Q. Chen, J. F. Scott, L. W. Martin, R. Ramesh, *Nature* **2016**, *530*, 198.

[14] Q. Zhang, L. Xie, G. Liu, S. Prokhorenko, Y. Nahas, X. Pan, L. Bellaiche, A. Gruverman, N. Valanoor, *Adv. Mater.* **2017**, *29*, 1702375.

[15] S. Das, Y. L. Tang, Z. Hong, M. A. P. Gonçalves, M. R. McCarter, C. Klewe, K. X. Nguyen, F. Gómez-Ortiz, P. Shafer, E. Arenholz, V. A. Stoica, S.-L. Hsu, B. Wang, C. Ophus, J. F. Liu, C. T. Nelson, S. Saremi, B. Prasad, A. B. Mei, D. G. Schlom, J. Íñiguez, P. García-Fernández, D. A. Muller, L. Q. Chen, J. Junquera, L. W. Martin, R. Ramesh, *Nature* **2019**, *568*, 368.

[16] J. F. Scott, *Ferroelectric Memories*, Vol. *3*, Springer, New York **2000**.

[17] A. Gruverman, D. Wu, H. Lu, Y. Wang, H. W. Jang, C. M. Folkman, M. Ye. Zhuravlev, D. Felker, M. Rzchowski, C.-B. Eom, E. Y. Tsymbal, *Nano Lett.* **2009**, *9*, 3539.

[18] V. Garcia, M. Bibes, *Nat. Commun.* **2014**, *5*, 4289.

[19] A. Chanthbouala, V. Garcia, R. O. Cherifi, K. Bouzehouane, S. Fusil, X. Moya, S. Xavier, H. Yamada, C. Deranlot, N. D. Mathur, M. Bibes, A. Barthélémy, J. Grollier, *Nat. Mater.* **2012**, *11*, 860.

[20] D. J. Kim, H. Lu, S. Ryu, C.-W. Bark, C.-B. Eom, E. Y. Tsymbal, A. Gruverman, *Nano Lett.* **2012**, *12*, 5697.

[21] A. Kakekhani, S. Ismail-Beigi, *ACS Catal.* **2015**, *5*, 4537.

[22] J. Hwang, J. Hwang, Z. Feng, N. Charles, X. R. Wang, D. Lee, K. A. Stoerzinger, S. Muy, R. R. Rao, D. Lee, R. Jacobs, D. Morgan, Y. Shao-Horn, *Mater. Today* **2019**, *31*, 100.

[23] S. V. Kalinin, S. Jesse, A. Tselev, A. P. Baddorf, N. Balke, *ACS Nano* **2011**, *5*, 5683.

[24] N. Domingo, I. Gaponenko, K. Cordero-Edwards, N. Stucki, V. Pérez-Dieste, C. Escudero, E. Pach, A. Verdaguer, P. Paruch, *Nanoscale* **2019**, *11*, 17920.

[25] Q. M. Zhang, H. Wang, N. Kim, L. E. Cross, *J. Appl. Phys.* **1994**, *75*, 454.

[26] D. Damjanovic, *Rep. Prog. Phys.* **1998**, *61*, 1267.

[27] T. Sluka, A. K. Tagantsev, P. Bednyakov, N. Setter, *Nat. Commun.* **2013**, *4*, 1808.

[28] G. Catalan, J. Seidel, R. Ramesh, J. F. Scott, *Rev. Mod. Phys.* **2012**, *84*, 119.

[29] P. Zubko, J. C. Wojdel, M. Hadjimichael, S. Fernandez-Pena, A. Sené, I. Luk'yanchuk, J.-M. Triscone, J. Íñiguez, *Nature* **2016**, *534*, 524.

[30] I. Luk'yanchuk, A. Sené, V. M. Vinokur, *Phys. Rev. B* **2018**, *98*, 024107.

[31] U. V. Waghmare, K. M. Rabe, *Phys. Rev. B* **1997**, *55*, 6161.

[32] P. Ghosez, E. Cockayne, U. V. Waghmare, K. M. Rabe, *Phys. Rev. B* **1999**, *60*, 836.

[33] P. Ghosez, K. M. Rabe, *Appl. Phys. Lett.* **2000**, *76*, 2767.

[34] D. D. Fong, G. B. Stephenson, S. K. Streiffer, J. A. Eastman, O. Auciello, P. H. Fuoss, C. Thompson, *Science* **2004**, *304*, 1650.

[35] G. B. Stephenson, M. J. Highland, *Phys. Rev. B* **2011**, *84*, 064107.

[36] C. Lichtensteiger, *Ph.D. Thesis*, Université de Genève **2006**.

[37] S. Jesse, A. P. Baddorf, S. V. Kalinin, *Appl. Phys. Lett.* **2006**, *88*, 062908.

[38] A. H. Vlooswijk, *Ph.D. Thesis*, University of Groningen **2009**.

[39] E. H. Smith, P. D. C. King, A. Soukiassian, D. G. Ast, D. G. Schlom, *Appl. Phys. Lett.* **2017**, *111*, 131903.

[40] C. Lichtensteiger, *J. Appl. Crystallogr.* **2018**, *51*, 1745.

[41] G. Catalan, B. Noheda, J. McAneney, L. J. Sinnamon, J. M. Gregg, *Phys. Rev. B* **2005**, *72*, 020102.

[42] P. V. Yudin, A. K. Tagantsev, *Nanotechnology* **2013**, *24*, 432001.

[43] S. Gottschalk, H. Hahn, S. Flege, A. G. Balogh, *J. Appl. Phys.* **2008**, *104*, 114106.

[44] R. V. K. Mangalam, J. Karthik, A. R. Damodaran, J. C. Agar, L. W. Martin, *Adv. Mater.* **2013**, *25*, 1761.

[45] M. Mayer, *Report IPP* **1997**, *9*, 67.

[46] G. H. Dai, P. W. Lu, X. Y. Huang, Q. S. Liu, W. R. Xue, *J. Mater. Sci.: Mater. Electron.* **1991**, *2*, 164.

[47] A. Chandrasekaran, *Ph.D. Thesis*, École polythechnique fédérale de Lausanne **2015**.

[48] Y. Yao, H. Fu, *Phys. Rev. B* **2011**, *84*, 064112.

[49] E. Cockayne, B. P. Burton, *Phys. Rev. B* **2004**, *69*, 144116.

[50] A. M. Glazer, S. A. Mabud, *Acta Cryst. B* **1978**, *34*, 1065.

[51] P. Ghosez, J.-P. Michenaud, X. Gonze, *Phys. Rev. B* **1998**, *58*, 6224.

[52] J. B. Neaton, C. Ederer, U. V. Waghmare, N. A. Spaldin, K. M. Rabe, *Phys. Rev. B* **2005**, *71*, 014113.

[53] N. Strkalj, C. Gattinoni, A. Vogel, M. Campanini, R. Haerdi, A. Rossi, M. D. Rossell, N. A. Spaldin, M. Fiebig, M. Trassin, unpublished.

[54] H. Wu, S. Lu, T. Aoki, P. Ponath, J. Wang, C. Young, J. G. Ekerdt, M. R. McCartney, D. J. Smith, *Adv. Mater. Interfaces* **2020**, *7*, 2000555.

[55] B. J. Rodriguez, C. Callahan, S. V. Kalinin, R. Proksch, *Nanotechnology* **2007**, *18*, 475504.

[56] M. Dawber, N. Stucki, C. Lichtensteiger, S. Gariglio, P. Ghosez, J.-M. Triscone, *Adv. Mater.* **2007**, *19*, 4153.

[57] P. Zubko, G. Catalan, A. K. Tagantsev, *Annu. Rev. Mater. Res.* **2013**, *43*, 387.

[58] C. Ophus, J. Ciston, C. T. Nelson, *Ultramicroscopy* **2016**, *162*, 1.

[59] M. Nord, P. E. Vullum, I. MacLaren, T. Tybell, R. Holmestad, *Adv. Struct. Chem. Imag.* **2017**, *3*, 9.